Characterization and Design of Capacitors in a N-capacitor Wireless Power Transfer System

Avani Ahuja, *Student Member, IEEE,* Jade Sund, *Student Member, IEEE,* and Samantha Coday, *Member, IEEE*
Department of Electrical Engineering and Computer Science, Massachusetts Institute of Technology

2026 IEEE Applied Power Electronics Conference and Exposition (APEC) | 979-8-3315-7544-1/26/$31.00 ©2026 IEEE | DOI: 10.1109/APEC51134.2026.11517082

***Abstract*—This work investigates the optimization and design of a 4-capacitor 4:1 resonant Dickson converter for capacitive wireless power transfer (WPT). A testbed that allows for the analysis of parasitic and coupling capacitances within a 4-capacitor plate setup is presented. A model for analyzing power transfer and resonance frequencies of the system is presented. The model is validated using ANSYS and the testbed across several electrical and mechanical parameters. This work looks to systematically characterize resonant and coupling capacitances and create a model to characterize power transfer capabilities, enabling the design of higher power density capacitive WPT systems.**

***Index Terms*—capacitive wireless power transfer, resonant Dickson converter**

I. Introduction

Wireless power transfer (WPT) has shown potential in highly efficient and power-dense electric vehicle charging, with potential safety benefits and decreased mechanical wear and tear [1], [2]. Many wireless charging systems use inductive WPT methods, but recent research has shown that capacitive WPT has the potential to achieve high efficiency, be effective for space-constrained applications, and be more misalignment-tolerant [3], [4]. Recent advances in capacitive WPT have focused on quantifying and optimizing around parasitics, enabling higher frequency and higher power transfer per unit area.

Previous work has investigated hybrid switched-capacitor converters for capacitive WPT [5], demonstrating a modified resonant Dickson converter [6], as shown in Fig. 1, that utilizes all of the capacitors for WPT. Moreover, it has been shown that this converter has the potential to transfer more power than the conventional two-level resonant converter, also known as the resonant capacitive coupling (RCC) converter [7]. Hybrid switched capacitor converters, such as the resonant Dickson converter, benefit from reduced switched stress resulting in improved thermal spreading and the potential to utilize lower voltage rated devices, which have improved figures-of-merit. In contrast to the RCC converter, the resonant Dickson converter has a conversion ratio of N, which is equal to the number of capacitors. The N-capacitor resonant Dickson converter has the potential to transfer up to $\frac{N^2}{16}$ times more power than the conventional approach as a result of a larger number of power-processing capacitors [5]. While these converters are theoretically capable of higher power transfer, in practice, N-capacitor converters can only achieve improved performance if the increased magnitude and complexity of the parasitics is addressed.

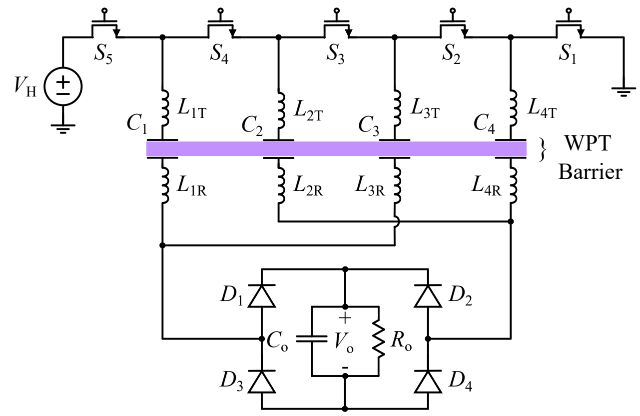

Fig. 1. Schematic of 4:1 resonant Dickson converter.

Characterizing the parasitics in N-capacitor converters is an important challenge to address, enabling designers to optimize the efficiency and determine the feasibility of N-capacitor WPT. Previous work has looked to minimize parasitic capacitances in two-capacitor approaches through symmetry, and careful capacitor characterization [8]. Several multi-capacitor topologies have been investigated due their potential for field cancellation [9], differential power processing [10], and partial power processing to limit fringing fields [11]. In these topologies, high parasitic capacitance as a result of the capacitor-to-capacitor interactions can lead to a significant reduction in power transfer [11], [12]. Therefore, developing an understanding of the parasitic capacitance in multi-capacitors systems is a crucial step in designing multi-capacitor WPT systems.

As shown in this work, the Dickson converter's operation is tightly coupled to the parasitics of its capacitors; therefore, understanding these parasitics is vital to determining converter operation. This work addresses these concerns by developing a model and testbed for N-capacitor WPT systems, enabling parasitic characterization and allowing designers to optimize and compare future capacitive WPT systems.

II. Converter Operation and Modeling

1) Converter Operation: The isolated variant of the resonant Dickson converter is shown in Fig. 1. While other capacitively-isolated hybrid switched -capacitor converters have been demonstrated [13]–[15], the resonant Dickson converter is unique as an isolation barrier can be implemented

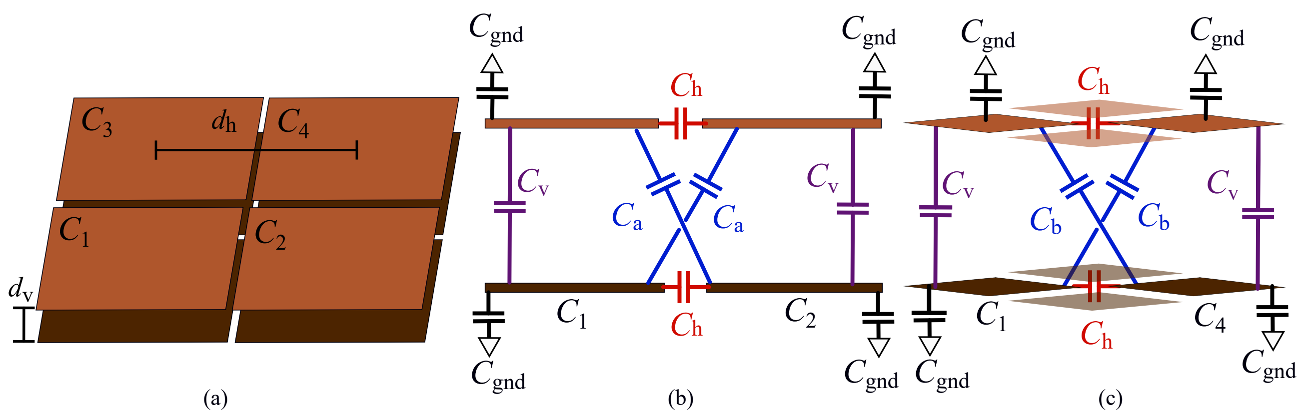

Fig. 2. (a) Capacitor plate orientations and relevant dimensions. (b) Various coupling and parasitic capacitances between adjacent capacitors. (c) Various coupling and parasitic capacitances between diagonally opposite capacitors.

between all of the capacitors, instead of only two. As a result, capacitive WPT is possible across all of the power processing capacitors. For initial analysis purposes, the capacitor and inductor values are assumed to be perfectly matched, e.g C_1 = $C_2 = \cdots = C_N \triangleq C$ and $L_{1T} = L_{1R} = L_{2T} = L_{2R} = \cdots = L_{NT} = L_{NR} \triangleq L$ and parasitics are ignored; therefore, the theoretical resonance frequency can be determined using $f_{\text{res,ideal}} = \frac{1}{2\pi\sqrt{2LC}}$. When the capacitors are balanced, the capacitors experience a mid-range voltage of $V_{C,i} = (N-i)V_L$ and the maximum switch voltage is $2V_L$. When employed as a WPT topology, the resonant Dickson converter's operation changes as a function of design and capacitor parasitics.

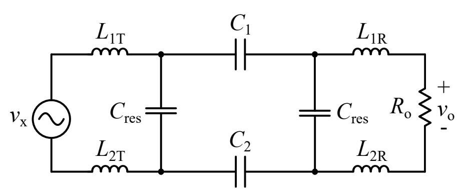

Fig. 3. Schematic of simplified converter model.

2) Simplified Converter Model: Once the converter is utilized for WPT applications, the capacitance dictating the resonant frequency is no longer C. Instead, higher-order parasitic capacitances start to dominate the resonant capacitance. Note, this effect is also observed in conventional capacitive WPT systems [8]. Since the converter's operation is significantly impacted by these parasitics, a simplified model is developed to take parasitic capacitances into account.

In this work, a 4-capacitor model is explored as it represents the simplest case, where N is the smallest even number greater than two. Even numbers are chosen here for symmetric plate layout. Figure 2 shows all of the relevant parasitics in a 4-capacitor design. In this work a greatly simplified model is employed, as shown in Fig. 3, in which C_{res} is a lumped capacitance. This model is shown for one pair of coupling capacitors; however, the other coupling capacitors can be modeled similarly. The resonant capacitance, C_{res}, is related to all of the parasitic capacitances for each capacitor, shown in Fig. 2, and dictates the resonant frequency. The inductors, C_1, and C_2 are the identically labeled components in Fig. 1. The input to this WPT cell, v_x, represents the sinusoidal voltage across the input of the cell. As the switch S_4 is at the input of the cell containing the capacitors C_1 and C_2, the sinusoidal voltage v_x can be approximated as the fundamental component of the switch voltage.

In this work, as demonstrated in Section IV, the coupling capacitance is significantly smaller than the resonant capacitance. Therefore, to simplify the model, the resonant capacitance C_{res} can be assumed to be much larger than $C_1 = C_2$ and $L_{1T} = L_{2T} = L_{1R} = L_{2R} = L$. Moreover, to simplify the model even further, it is assumed the effective parasitic capacitance seen by each plate is effectively equal. Using this simplified model, the transfer function of (1) can be derived for the topology of Fig. 3.

$$\left|\frac{v_o}{v_x}\right| = \frac{s\frac{R_o}{2L}}{s^2 + s\frac{R_o}{2L} + \frac{1}{LC_{\text{res}}}} \tag{1}$$

Therefore, the modeled resonant frequency is shown in (2).

$$f_{\text{res,m}} = \frac{1}{2\pi\sqrt{LC_{\text{res}}}} \tag{2}$$

While the value of the resonant capacitor is responsible for setting the resonant frequency, the electric fields in the coupling capacitors are still the mode of WPT in the system. The follow sections will validate this model as well as discuss its limitations.

III. Testbed Design

The testbed was designed to allow for the investigation of various parasitics by allowing the variation of both electrical and mechanical parameters. The testbed is used to vary different mechanical setups, load resistance, inductance, distance from plate to shield, horizontal and vertical gap distances between capacitors and the effective C_{oss} of the switch.

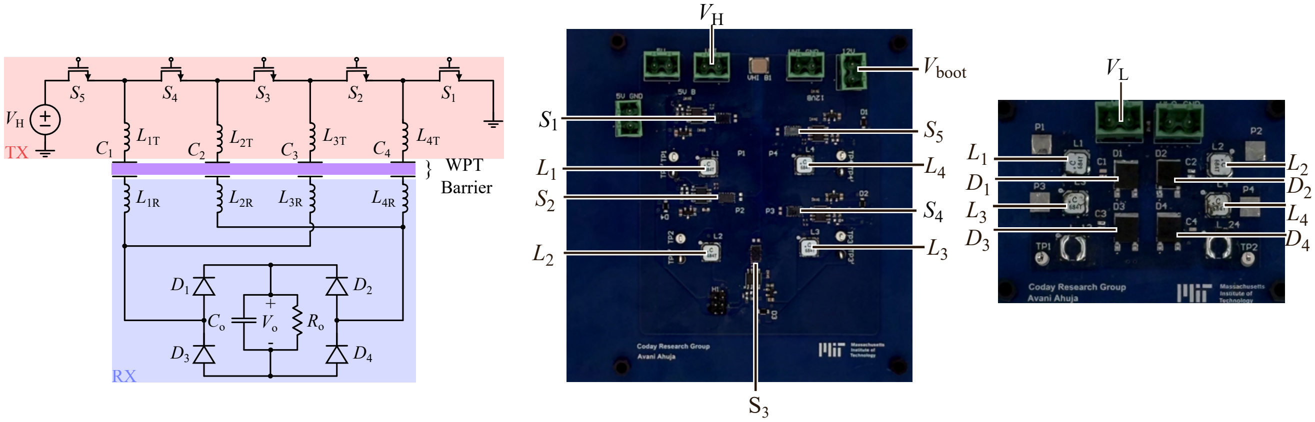

(a) (b) (c)

Fig. 4. (a) Schematic of a 4:1 resonant Dickson converter with the transmit (TX) circuit highlighted in red and receive (RX) circuit highlighted in blue. (b) Transmit board. (c) Receive board.

A. Electrical Setup

1) Board Design: To further validate and characterize the parasitic capacitance, a 4:1 resonant Dickson converter was designed. Components selected for the converter are listed in Table I. The transmit and receive boards are shown in Fig. 4b and Fig. 4c, respectively. To minimize the commutation loop and thereby the parasitic inductance, the switching loop is shaped like a U. Future implementation may employ decoupling capacitors to further decrease the commutation loop. The boards were designed to allow for the addition of capacitance in parallel with the switches to increase the effective C_{oss}. Switches were selected with increased voltage headroom as a result of expected increase in switch stresses when capacitances are imbalanced, and when the converter is operated significantly far from resonance.

A cascaded bootstrap was employed to drive the switches on the transmit side, minimizing gate drive area and loss [16]. The schematic of the cascaded bootstrap is shown in Fig. 5.

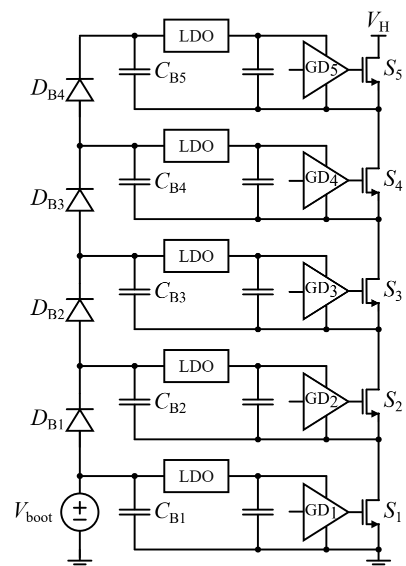

Fig. 5. Schematic of cascaded bootstrap circuit used for the transmit board.

TABLE I
COMPONENTS SELECTED FOR THE HARDWARE PROTOTYPE.

Components	Part Number	Description
S_1 - S_5	EPC2304	200 V, 102 A
L_{1T} - L_{4T}, L_{1R} - L_{4R}	LPS6225	Various Values
Gate Driver	SI8271GB-IS	5 V, 4 A
D_1-D_4	MBRAD10200H	200 V, 10 A, $V_f = 880$ mV
D_{B1}-D_{B4}	RF071MM2STR	200 V, 700 mA
LDO	TS3480CX50	5 V Output

B. Mechanical Setup

Several mechanical setups were fabricated to allow for the variation of parameters d_h, d_v, and d_s, as shown in Fig. 6. The mechanical jig was 3D printed with polylactic acid (PLA), and nylon screws were used to secure the jig together, as shown in Fig. 7. The capacitor plates are attached to the acrylic plates via Kapton tape. An aluminum shield was integrated on both the transmit and receive side and connected to the respective grounds to define a dominant capacitance to ground, C_{gnd}, and to represent system chassis. The terminal block allowed for the ease of substitution of different plate orientations and electrical setups.

C. ANSYS Simulations

The capacitance values captured in Fig. 2 were determined in simulation using Maxwell 3D. The order of magnitude of the ground to shield capacitance C_{gnd} in the ANSYS simulation was significantly higher than the cross plate capacitances C_h, C_v, C_a, and C_b shown in Fig. 2. Therefore, the resonant capacitance can be approximated as $C_{res} = \frac{C_{gnd}}{2}$, as

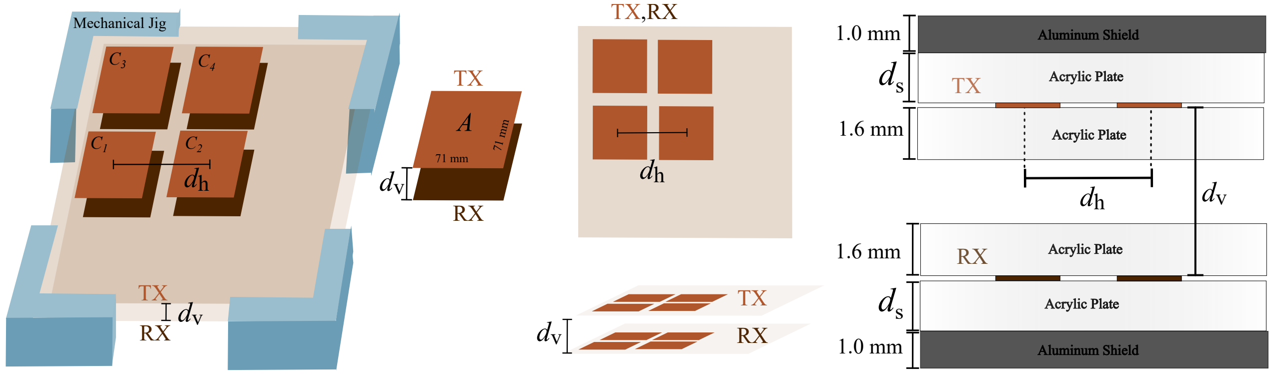

(a) (b) (c)

Fig. 6. (a) Visualization of capacitor plates and relevant parameters. (b) Visualization of plate movement horizontally and vertically. (c) Stackup of capacitive plates, acrylic, and aluminum shields.

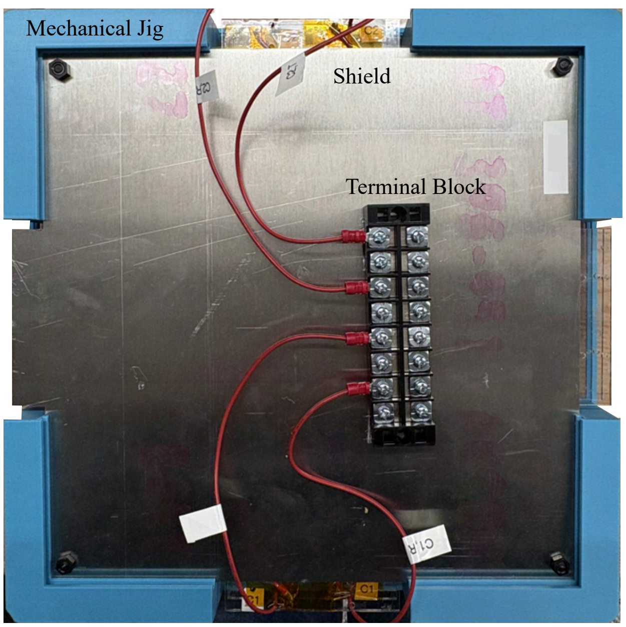

Fig. 7. Photograph of mechanical jig and shield with terminal block.

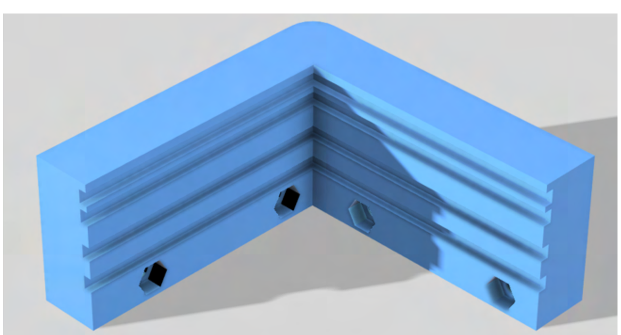

Fig. 8. A CAD rendering of mechanical jig. The notches in the jig allow for the variation of d_v.

the two ground capacitors are effectively in series. Note, in the simulation results there are small deviations between the measured parasitic capacitance seen by each plate, these values were averaged for more direct comparison to the experimental results. The results of the simulation are further used in the model as a comparison point for the experimental results shown in the following section.

IV. Results

All setups were tested with $V_{\mathrm{H}} = 15$ V; therefore, assuming ideal 4:1 operation, an output voltage of 3.75 V is expected. This decreased voltage compared to the switch rating is chosen to allow for effective frequency sweeps without exceeding the voltage of the switches. Frequency sweeps were conducted using a Yokagawa WT5000 power analyzer. The microcontroller adjusted the frequency of the converter, in a sweep from 100 kHz to 1 MHz, while the power analyzer measured the frequency and the output voltage of the system. At each frequency step, at least 20 data points were collected and averaged. The baseline measurements were conducted with the parameters shown in Table II, and the resulting frequency sweep measurements are shown in Fig. 11a. To determine the primary resonant frequency of the setups, the maximum output voltage was used.

TABLE II
Baseline Parameters

L	d_s	R_o	d_h	d_v	C_{oss}
0.68 mH	1.0 mm	560 Ω	160 mm	10 mm	EPC 2304

These parameters were chosen to increase the resolution of the measured capacitance. The resonance frequency of 600 kHz allows for an advantageous tradeoff between decreased gain due to switching losses at higher frequencies, and lower resolution in capacitance values at lower frequencies.

A. Reproducibility

A significant challenge in multi-capacitor setups is reproducibility. Several tools are employed in this work to ensure

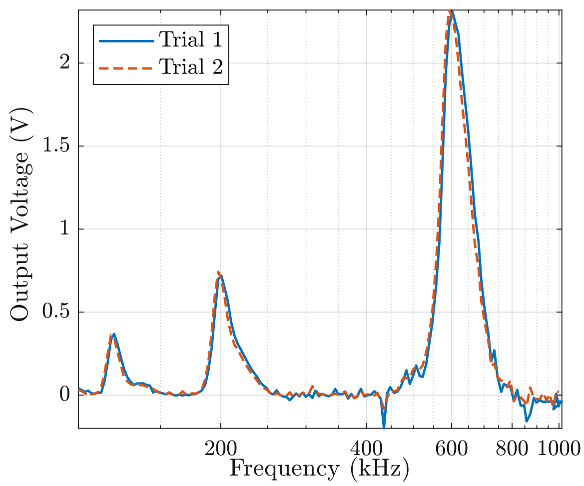

Fig. 9. Data before and after re-assembling a setup.

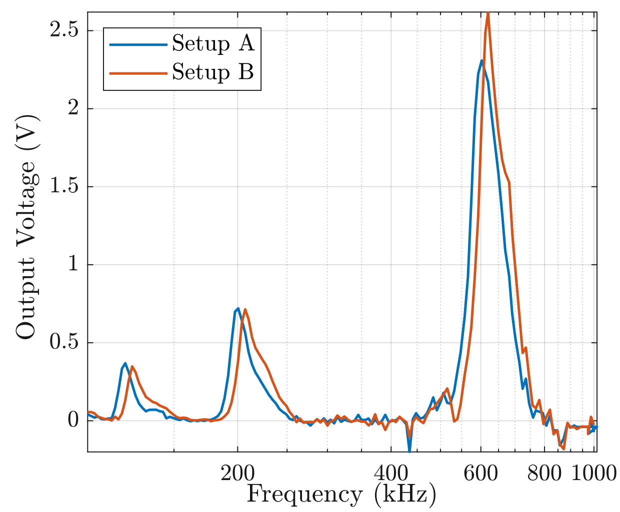

Fig. 10. Results of two separate mechanical setups with the same electrical setup.

repeatability between various mechanical setups, including decoupling the electrical circuit from the mechanical setup to prevent the variability that arises with directly soldering the PCBs to the plates, as shown in Fig. 7. In addition, 3D printed stencils for plate orientations relative to the shield and a custom mechanical jig design that minimizes 3D printing tolerances are implemented, as shown in Fig. 8. Of note, copper tape is used to connect the copper plates to the terminal block that interfaces the electrical and mechanical setups, and relief holes are added in the acrylic to relieve strain placed on these connections and maximize stability. When the setups are completely disassembled, tested with other configurations, and then re-assembled, the results are nearly identical, as shown in Fig. 9. With two separate setups, built of different mechanical jigs, and with alternate plates, the tolerance in mechanical assembly is shown in Fig 10. The small deviation in voltage gain and frequency is likely due to plate size tolerances and small alignment mismatch. The discrepancy in C_{res} between the two setups was 3 pF, which corresponds to a tolerance of approximately 1 mm.

B. Validation of C_{res}

1) Baseline Setup: In this section, C_{gnd} is validated as the dominant resonant capacitance as assumed in the model in Section III-C for the baseline setup. ANSYS simulations yield an averaged capacitance to the shield across all capacitors of 96 pF. The modeled and the experimental frequencies and capacitances are shown in Table III. From these results, it can be seen that at this particular inductance value, C_{res} is dominated by the system's capacitance between capacitor plates and the shield closest to the respective plate, modeled by C_{gnd}, as shown in Fig. 2. Capacitances to shield were an order of magnitude larger than the other parasitic capacitances seen in Fig. 2 in ANSYS simulations. As such, it can be validated that C_{res} is dominated by C_{gnd} for this system.

TABLE III
EXPERIMENTAL AND THEORETICAL RESONANCE FREQUENCIES AND CAPACITANCES FOR THE BASELINE SETUP.

L	$f_{\text{res,e}}$	$C_{\text{res,e}}$	$f_{\text{res,m}}$	$C_{\text{res,m}}$
0.68 mH	602 kHz	51 pF	629 kHz	48 pF

2) Changing inductance (L): As shown in (2), increasing the inductance results in a decrease in resonance frequency when C_{res} is held constant. While keeping gap distances d_{h}, d_{v}, and d_{s}, as well as R_{o}, constant and varying inductance, the measured output voltage is shown in Fig. 11b. The experimental and modeled resonance frequencies are compared to determine the effects of C_{gnd} on C_{res}. Table IV compares the modeled resonant frequencies $f_{\text{res,m}}$ derived using (1) to experimentally determine resonance frequencies $f_{\text{res,e}}$.

TABLE IV
EXPERIMENTAL AND MODELED FREQUENCIES AND CAPACITANCES FOR CHANGING INDUCTANCE

L	$f_{\text{res,e}}$	$C_{\text{res,e}}$	$f_{\text{res,m}}$	$C_{\text{res,m}}$
0.68 mH	602 kHz	51 pF	629 kHz	48 pF
1.5 mH	402 kHz	52 pF	420 kHz	48 pF
4.7 mH	216 kHz	58 pF	239 kHz	48 pF

The resonance frequency of the dominant peak decreases as inductance increases, as shown in Fig. 11b, which aligns with the results of the model of the resonant Dickson converter as demonstrated in Section II-2. Hence, at these inductance values and at these frequencies, C_{gnd} continues to constitute the majority of C_{res}.

3) Varying the distance from plate to shield (d_s): The distance between the capacitors and the closest shield to each capacitor was doubled to determine the effects of varying C_{gnd} on the performance of the system. The measured output voltage is shown in Fig. 11c. The discrepancy between the experimental and theoretical resonance frequencies shown in Table V is due to C_{gnd} no longer dominating C_{res} as the resonant frequency increases. This test demonstrates the limitation of the simplified model, as it relies on the capacitance of the shield to be significantly greater than the coupling capacitance to calculate the resonant frequency. Future work may investigate how to derive a simplified model for when the shield capacitance varies in magnitude with respect to the coupling capacitor and the effect this has on the resonant frequency and power transfer capability.

TABLE V
EXPERIMENTAL AND THEORETICAL RESONANCE FREQUENCIES AND CAPACITANCES FOR VARYING d_{s}.

d_{s}	$f_{\mathrm{res,e}}$	$C_{\mathrm{res,e}}$	$f_{\mathrm{res,m}}$	$C_{\mathrm{res,m}}$
1.6 mm	602 kHz	51 pF	629 kHz	48 pF
3.2 mm	681 kHz	40 pF	863 kHz	25 pF

C. Power Transfer Capability

1) Varying the load resistance (R_o): To evaluate the effect of load on the system, several R_{o} values were tested. As shown in Fig. 11d, the measured output voltage decreases as R_{o} decreases. Note, these measurements were taken with $d_{\mathrm{s}} = 3.2$ mm. As R_{o} decreases, the total current of the system increases, increasing current-related losses as a result of various parasitic resistances and negatively affecting the power transfer of the system. Note, as the load resistance becomes very large, the measured output voltage exceeds the expected maximum output voltage, as predicted by the simplified model. This indicates the increased effect of the coupling capacitors on the voltage gain. As expected, the magnitude of the load resistance does not impact the resonant frequency.

2) Varying the horizontal distance (d_h): Horizontal distances were varied to validate the assumption that C_{gnd} dominates C_{res}. ANSYS simulations showed that plate-to-plate capacitances between adjacent plates, shown as C_{h} in Fig. 2, are several orders of magnitudes less than C_{gnd} and thus should not have a large effect on the resonant frequency. As shown in Fig. 11e, power transfer decreases as d_{h} decreases but $f_{\mathrm{res,e}}$ is not affected. As the horizontal gap distance is increased, the plate-to-plate capacitance and diagonal capacitance is significantly reduced. Higher power transfer is thus anticipated as the horizontal gap distance is increased.

3) Varying the vertical distance (d_v): The vertical distances were varied to validate the assumption that C, or the coupling capacitance, does not affect the resonance frequency of the system. As d_{v} increases, C decreases, but the resonance frequency should not change as predicted by the model. Experimentally, as shown in Fig. 11f, as the vertical gap distance is increased, C decreases, reducing the power transfer capability of the system. Note, the experimental resonance frequency slightly shifts as the vertical distance is varied, indicating that the coupling capacitance does have a small effect on the the actual frequency. Interestingly, at a d_{v} of 16 mm, the output voltage increases compared to smaller distances. This result is not supported by the simplified model and is likely due to the higher order effects of the coupling and resonant capacitors, as well as converter loss.

4) Changing the switch output capacitance (C_{oss}): In this setup the switch output capacitance, C_{oss}, is significantly larger than the resonant capacitance. Therefore, tests to determine the effects of switch parasitic capacitance on power transfer and resonance frequency were conducted by adding a capacitance in parallel with each switch on the transmit board. As shown in Fig. 12, power transfer is decreased due to increased switching losses. However, the resonance frequency also decreases, indicating that C_{oss} contributes to C_{res}, but is not currently accounted for by the simplified model presented here.

V. CONCLUSION

In this work, a highly reproducible testbed was developed to evaluate the parasitics in a 4:1 resonant Dickson converter employed for capacitive WPT. The testbed allowed for varying a range of electrical and mechanical parameters to validate a simplified model that was developed to determine the dominant capacitance for resonance frequency and WPT. Experimental results indicated that C_{gnd} was the dominant capacitance in C_{res} for a gap to shield distance of 1 mm while varying parameters such as inductance, horizontal gap distances, and vertical gap distances. The model does not account for C_{oss} of the switches in the system or change in operation as C_{res} and C approach similar orders of magnitude. This work indicates that designers should optimize for large horizontal gap distances given constraints of their given application.

VI. ACKNOWLEDGEMENTS

The authors would like to thank Andre Rodriguez for his valuable contributions to the mechanical setup and design.

REFERENCES

[1] S. Inamdar and J. Fernandes, "Review of wireless charging technology for electric vehicle," in *2022 IEEE 10th Power India International Conference (PIICON)*, pp. 1–5, 2022.

[2] J. Yan, M. J. B. A. Aziz, and N. R. N. Idris, "A communication-less constant power bidirectional double-sided lcc inductive wireless power transfer battery charger with triple-phase-shift optimal efficiency control," in *2025 IEEE Energy Conversion Congress Exposition Asia (ECCE-Asia)*, pp. 1–6, 2025.

[3] S. Sinha, S. Maji, and K. K. Afridi, "Comparison of large air-gap inductive and capacitive wireless power transfer systems," in *2021 IEEE Applied Power Electronics Conference and Exposition (APEC)*, pp. 1604–1609, 2021.

[4] C. Lecluyse, B. Minnaert, and M. Kleemann, "A review of the current state of technology of capacitive wireless power transfer," *Energies*, vol. 14, no. 18, 2021.

[5] J. Sund and S. Coday, "A hybrid switched capacitor converter enabling capacitive-based wireless power transfer for battery charging applications," in *2025 IEEE Applied Power Electronics Conference and Exposition (APEC)*, pp. 971–977, 2025.

[6] A. Jackson, N. M. Ellis, and R. C. N. Pilawa-Podgurski, "A capacitively-isolated dual extended lc-tank hybrid switched-capacitor converter," *IEEE Applied Power Electronics Conference and Exposition (APEC)*, vol. 15, pp. 1279 –1283, Mar. 2022.

[7] D. Etta, M. A. Dominguez, S. Maji, S. S. Rashid, and K. K. Afridi, "A 10.4-kw high-power-transfer-density multi-mhz capacitive wireless power transfer system for ev charging utilizing stacked-inverter stacked-rectifier architecture," in *2025 IEEE Applied Power Electronics Conference and Exposition (APEC)*, pp. 1640–1645, 2025.

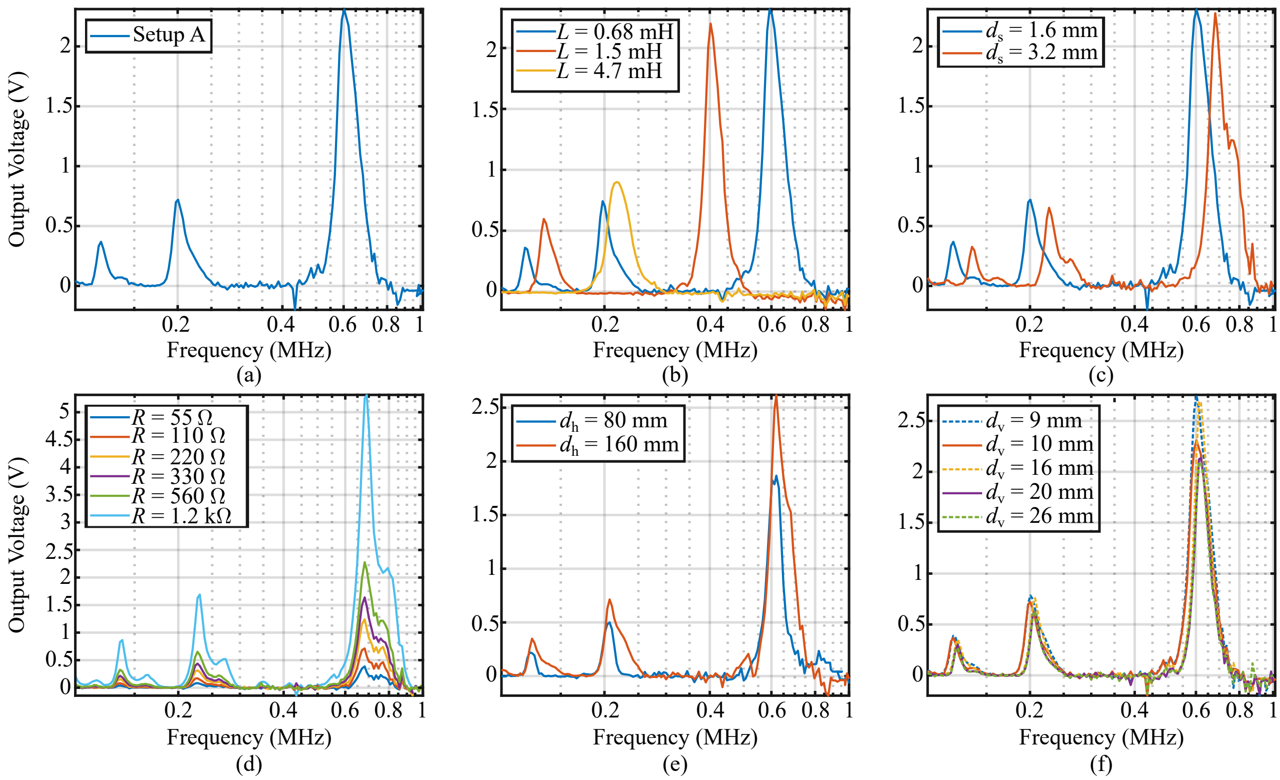

Fig. 11. Results of varying electrical and mechanical parameters in the capacitive WPT system. (a) Baseline setup used to validate C_{res}. (b) Varying inductances. (c) Varying distance to shield (d_s). (d) Varying load resistance (R_o). (e) Varying horizontal gap distance (d_h). (f) Varying vertical gap distance (d_v).

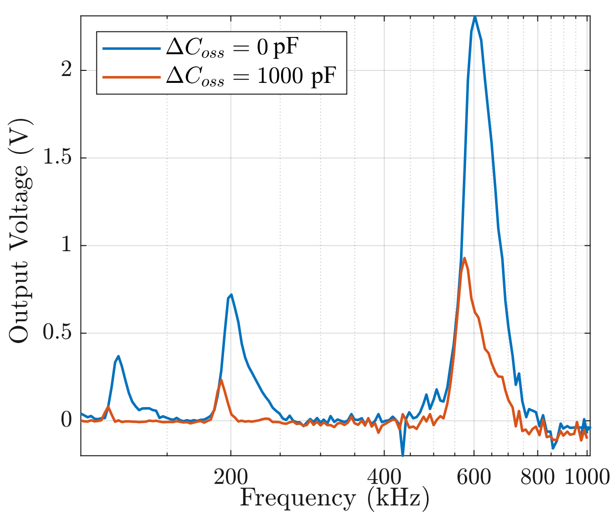

Fig. 12. Results with the addition of a capacitor in parallel with the C_{oss} of the switch.

[8] S. Sinha, A. Kumar, B. Regensburger, and K. K. Afridi, "A new design approach to mitigating the effect of parasitics in capacitive wireless power transfer systems for electric vehicle charging," *IEEE Transactions on Transportation Electrification*, vol. 5, no. 4, pp. 1040–1059, 2019.

[9] S. S. Rashid, D. Etta, M. Ciabattoni, F. Monticone, and K. K. Afridi, "Reduced-fringing-field multi-mhz capacitive wireless power transfer system using metasurface-based couplers with active field cancellation," in *2025 IEEE Applied Power Electronics Conference and Exposition (APEC)*, pp. 1646–1652, 2025.

[10] M. Liao, T. Sen, Y. Elasser, H. A. Al Hassan, A. Pigney, E. Knapp, and M. Chen, "Uav fleet charging on telecom towers with differential capacitive wireless power transfer," *IEEE Transactions on Power Electronics*, vol. 40, no. 4, pp. 6370–6384, 2025.

[11] A. Dixit and S. Sinha, "An optimized two-module capacitive wireless power transfer system for ev charging," in *2024 IEEE Energy Conversion Congress and Exposition (ECCE)*, pp. 2413–2417, 2024.

[12] W. Zhou, Q. Gao, R. Mai, Z. He, and A. P. Hu, "Design and analysis of a cpt system with extendable pairs of electric field couplers," *IEEE Transactions on Power Electronics*, vol. 37, no. 6, pp. 7443–7455, 2022.

[13] J. Sund, A. Rodriguez, E. Rabenold, and S. Coday, "The design and analysis of a capacitively-isolated series-parallel converter," in *2025 IEEE 26th Workshop on Control and Modeling for Power Electronics (COMPEL)*, pp. 1–8, 2025.

[14] E. Rabenold, R. Jerez, and S. Coday, "The analysis and design of a resonant capacitively-isolated cockcroft-walton converter," in *2025 IEEE Applied Power Electronics Conference and Exposition (APEC)*, pp. 2249–2253, 2025.

[15] R. S. Bayliss, L. Horowitz, and R. C. N. Pilawa-Podgurski, "Design and analysis of a high step-down ratio capacitively-isolated flying capacitor multilevel resonant converter," in *2025 IEEE 26th Workshop on Control and Modeling for Power Electronics (COMPEL)*, pp. 1–6, 2025.

[16] Z. Ye, Y. Lei, W.-C. Liu, P. S. Shenoy, and R. Pilawa-Podgurski, "Improved bootstrap methods for powering floating gate drivers of flying capacitor multilevel converters and hybrid switched-capacitor converters," *IEEE Transactions on Power Electronics*, vol. 35, no. 6, pp. 5965–5977, 2020.